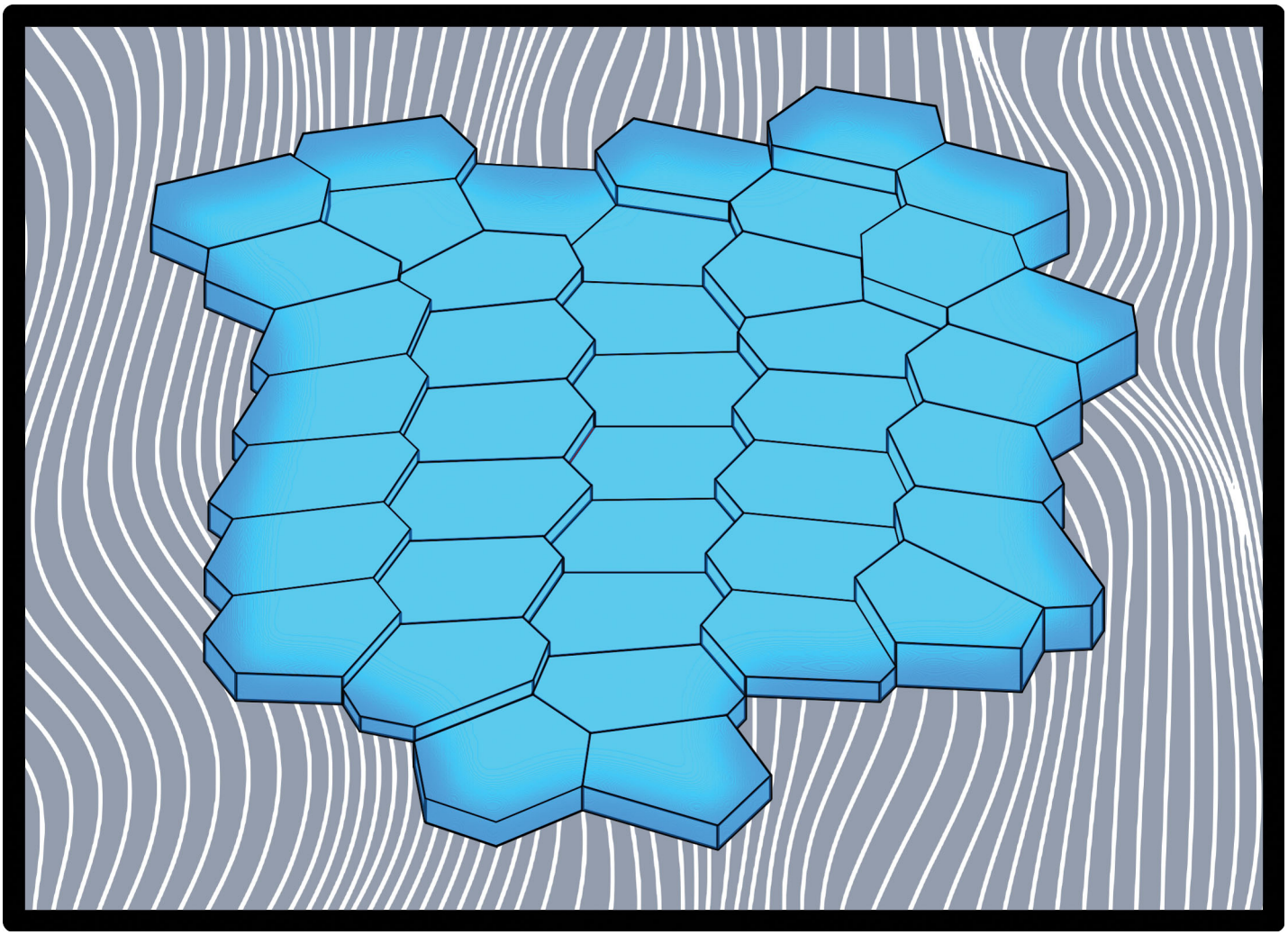

Showcasing research from the Department of Applied Physics, Aalto University School of Science, Finland.

Vibration controlled foam yielding

Foams yield in local topological rearrangement events known as T1 events. External mechanical vibration excites the sample foam, decreasing the local yield threshold and enhancing the flow of foam. The flow resistance was found to decrease with frequency up to a maximum value after which flow remained constant. Such a decrease can be modelled using the Guzman–Arrhenius type of energy landscape model.

As featured in:

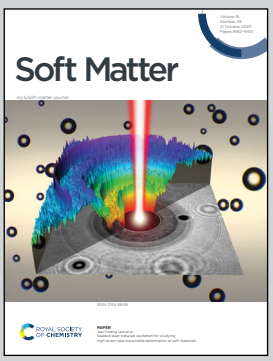

See Leevi Viitanen *et al.*, *Soft Matter*, 2020, **16**, 9028.

ROYAL SOCIETY OF CHEMISTRY

rsc.li/soft-matter-journal

Registered charity number: 207890

Soft Matter

PAPER

View Article Online
View Journal | View Issue

Cite this: *Soft Matter*, 2020, **16**, 9028

Vibration controlled foam yielding†

Oona Rinkinen, Leevi Viitanen, * Jonatan R. Mac Intyre, Juha Koivisto, Antti Puisto and Mikko Alava

Received 13th March 2020,
Accepted 6th August 2020

DOI: 10.1039/d0sm00439a

rsc.li/soft-matter-journal

In rheological terms, foams are time independent yield stress fluids, displaying properties of both solid and liquid materials. Here we measure the propagation of a 2D dry foam in a radially symmetric Hele-Shaw cell forcing local yielding. The yield rate is manipulated by mechanical vibration with frequencies from 0 to 150 Hz. The flow speed is then extracted from the video stream and analyzed using digital image correlation software. The data are modeled analytically by a Guzman–Arrhenius type of energy landscape where the local yielding of foam correlates with the number of oscillations, *i.e.* attempts to cross the energy barrier. The model is confirmed in an auxiliary experiment where the vibrated foam stays in its flowing state at the same small driving pressures, where the flow of the unvibrated foam ceases. We conclude that the yield stress behaviour of foams under an external perturbation can be summarized using a simple energy landscape model. The vibration affects the films causing the stress to occasionally and locally exceed the yield threshold. This, thus, prevents the foam from jamming as in a static configuration even when the global driving is below the yield point of the foam.

1 Introduction

The local yielding of amorphous materials, specifically foams, its observation and manipulation are hot topics involving basic science[1–6] and heavy industry.[7–9] Foams can be used to study the yielding of soft matter[10] and flow in complex geometries[11–14] as well as hidden correlations *via* hyperuniformity, a concept that reveals systems without long-range number density fluctuations from random (poissonian) ones.[15] The related industrial applications include topics from foam forming,[16] imbibition[17] and mass transport[18] covering significant industries in manufacturing, filtration and energy.

The cross-disciplinary nature of the viable raw materials and their complex interactions make foams an extremely intriguing playground for soft matter due to their stability and manipulation.[19,20] Here, we consider 2D dry aqueous foams consisting of air filled gas pockets surrounded by surfactant layers embedded in water. The gas fraction is high and the individual bubbles acquire a polygonal shape minimizing the surface tension.[21,22]

At the global scale, the stress–strain response of such foam flow can be approximated using continuum models.[12] On a local scale, the bubble films create a solid-like structure with a complex energy landscape that changes its configuration as the foam flows[2] are observed as a series of local yield events. These plastic rearrangements are either neighbor swap events of T1 type or coarsening events of T2 type[23,24] triggered by shear[25–27] or other external stimuli.

Here, we use mechanical vibrations to manipulate the foam behavior, following the footsteps of granular flow[28–34] and granular temperature.[35–38] While in granular media the external vibration affects the particles, not the interstitial medium, in foams the bubbles are virtually inertialess, and presumably the vibration affects the interstitial medium between the lightweight bubbles, instead. Thus, here we can study the restructuring events of massless spheres, or polyhedrons to be more precise. One should note the contrast to granular media since in dry foams the local density is preserved.

The outline of the paper is as follows. First, we introduce or revisit a 2D circular Hele-Shaw cell[2] that ensures shear strain with the continuous production of local yield events while involving no boundary effects, such as strain localization close to walls or periodic yield events.[39] The setup is such that it can be conveniently vibrated at various frequencies. Second, we explain how the local and global velocities are extracted from the system using machine vision software. Then, we interpret our results in the perspective of the Guzman–Arrhenius type of energy landscape model. Finally, we conclude that the vibrations affect the local yielding and confirm this by performing two auxiliary experiments in a separate geometry possessing different boundary conditions.

Aalto University, School of Science, Department of Applied Physics, P.O. Box 11100, 00076 Aalto, Finland. E-mail: leevi.viitanen@aalto.fi, jonatan.macintyre@aalto.fi, juha.koivisto@aalto.fi, antti.puisto@aalto.fi, mikko.alava@aalto.fi

† Electronic supplementary information (ESI) available: See https://youtu.be/NGE33R5fW5w. See DOI: 10.1039/d0sm00439a

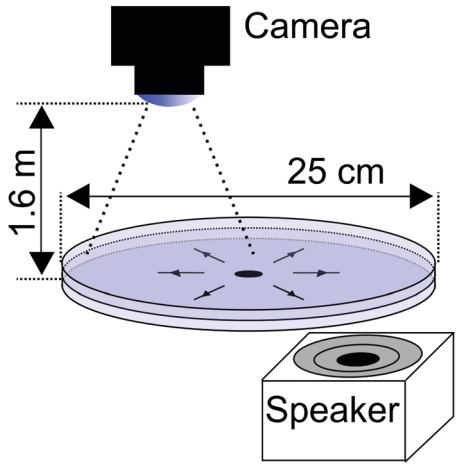

Fig. 1 Schematic illustration of the experimental setup. A Hele-Shaw cell of diameter d = 25 cm and gap thickness h = 0.75 mm is placed at a distance L = 2.5 cm from the loudspeaker. The foam enters the cell from below, from a 6 mm inlet located at the cell center. The flow is recorded using a camera placed to 1.6 m above the cell.

2 Methods

The experiments were performed in a two-dimensional Hele-Shaw cell made from transparent PMMA plates. The setup confines a single layer of bubbles between two parallel plates as sketched in Fig. 1. We use a soap-water solution that contains 2.5 wt% of commercial Fairy dishwashing liquid. The viscosity of the liquid is η = 1.1 mPa s measured using an Anton Paar 302 rheometer in the strain rate range of $\dot{\gamma}$ = 0.1 to 100 1 s^{-1}. The solution was pushed towards the Hele-Shaw cell through a pipe using constant air pressure ΔP = 15.4 kPa. This drop in pressure is due to the resistance of the experimental setup and the resistance of the flowing foam. The foam was formed by injecting air in the liquid through a needle and fed into the system though a 6 mm inlet hole located at the center of the cell. This created a radial flow towards the open edges of the cell.

The system was agitated using sinusoidal acoustic waves generated by a Yamaha NSSW200 loudspeaker. The frequency of vibration was varied over the range of 0–150 Hz. The acoustic waves generated by the speaker vibrate the rigid Plexiglas walls of the measurement setup creating an uniform vibration within the measurement area shown in Fig. 2b with an orange square. The sound pressure level was measured using the IEC 61672-1 class 2 sound level meter located one meter above the speaker. The average sound pressure value was L_p = 73 ± 5 dB or p_L = 89 mPa, which depends on the relative position of the sound meter with respect to the subwoofer. This value was chosen to maximize the effects of excitation while still being experimentally feasible. The flow rate measurement was recorded using a Canon EOS M3 digital camera with the sampling frequency of 25 Hz. The recorded videos were then converted to still images with a 40 ms time difference and cropped to 680 × 680 pixels corresponding to a 27 × 27 mm square illustrated in Fig. 2a.

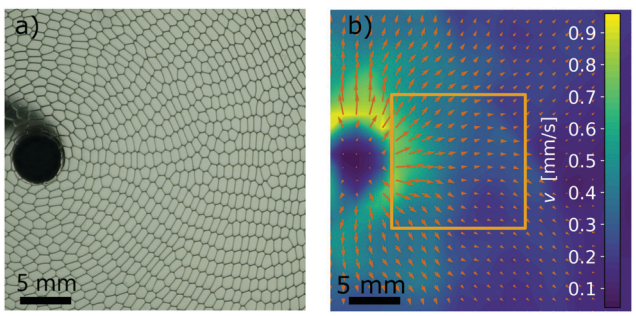

Fig. 2 (a) Raw image recorded by the camera during the foam flow. A good texture in the image allows us to use the PIVlab algorithm.[40] (b) The calculated flow field has a radial dependence seen as a swift change from yellow to blue. The orange square of size $\ell \times \ell$ delimits the analysis area. Here ℓ = 320 pixels = 13 mm. All the data points are not shown for reasons related to image clarity. The figure shows an experiment where the foam is vibrated with 30 Hz frequency.

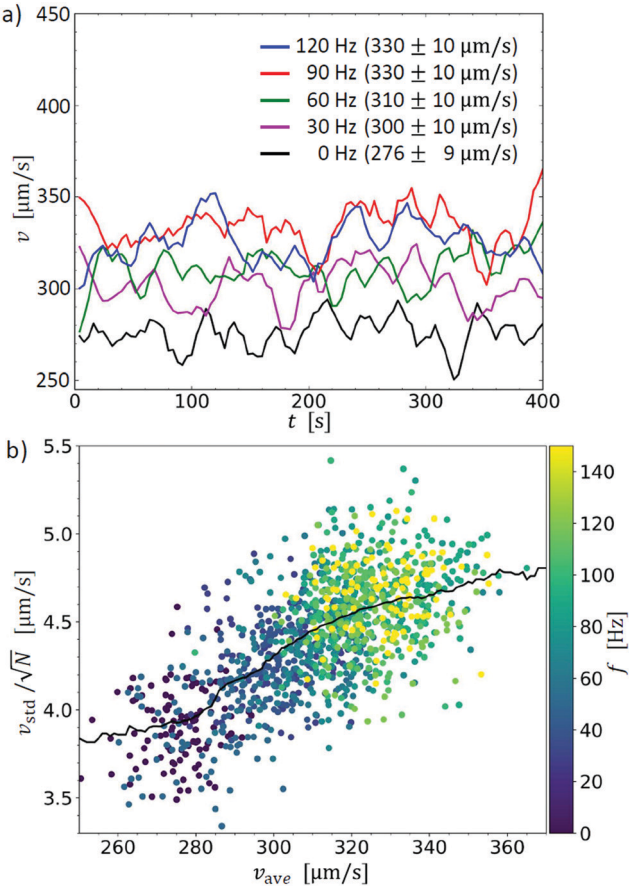

Fig. 3 (a) Foam flow rate as a function of time for different frequencies. The legend reports the average velocity and standard deviation of each curve in parenthesis. (b) The instantaneous standard deviation and average velocity both increase as a function of frequency. The normalized standard deviation can be used as an error estimation as well as an indicator of increasing fluctuations. The black line is a running median along the x-axis with the window size v_{ave} = 20 μm s^{-1}.

3 Results

3.1 Raw data

Raw image data from the experiment are shown in Fig. 2a. The foam is rather monodisperse having the average effective radius

and standard deviation R_{eff} = 0.73 ± 0.02 mm and liquid fraction ϕ_ℓ = 0.2 measured by calculating the area of bubbles and films by thresholding the grayscale images to black (liquid) and white (gas) binary images. To determine the velocity fields in a flowing foam, a digital Particle Image Velocimetry (PIV) technique was used.[40] The algorithm uses two sequential images with a time interval Δt as inputs and returns the displacement in an evenly spaced square grid as vectors and the corresponding interpolated velocity field as a contour plot as illustrated in Fig. 2b. The velocity is directed radially away from the inlet. As shown in Fig. 2b, the velocity magnitude is the largest around the inlet at the center and decreases towards the edge, also inside the analysis area.

The average velocity v_{ave} is the mean speed within the region of interest (orange square in Fig. 2) throughout the 400 s experiment. One value of v_{ave} and its corresponding standard deviation v_{std} consist of $N = 38 \times 38 = 1444$ values provided by the PIV algorithm for each time step. As a result, we determine the flow rate as a function of time for different frequencies as shown in Fig. 3a. For clarity, only selected frequencies are shown in this plot. As the figure shows, the mean flow rates differ for different frequencies. Hence, it can be assumed that the frequency of the vibration affects the flow rate of the foam.

In Fig. 3b, the computed standard deviation and average velocities are shown for a reduced data set: each dot represents one time step taken Δt = 4 s apart. The black curve represents a running median where a Δv_{ave} = 20 μm s^{-1} window is moved along the x-axis. The color code shows the frequency used in the experiments. The average velocity and standard deviation both increase with frequency. The larger standard deviation indicates a wider velocity distribution with localized regions of high velocity. The vibration is thus expected to trigger local rearrangements. Next we examine an Arrhenius-like energy barrier model where the vibration triggers the local yielding increasing the flow rate.

3.2 Guzman–Arrhenius model

Let us consider the foam flow in a Hele-Shaw cell in the continuum. Applying the arguments of ref. 41 one arrives at the conclusion that the frictional dissipation can be neglected compared to internal stresses of an elastoviscoplastic material. The resulting foam flow can be described then by Darcy's law for non-Newtonian fluids such as when the flow behaviour is represented by a Herschel–Bulkley model characterized by the fluid parameter, n. Foams are typically shear thinning, thus the exponent, n is less than 1. Working at a constant driving pressure ΔP we next assume that the viscosity is the sum of the continuum fluid-like global viscosity η_g and a local structural viscosity η_l, which can be affected by external inputs such as mechanical vibrations.

We then use the extended Darcy's law for non-Newtonian fluids,[41] which implies that

$$Q = C'\frac{(\Delta P)^{1/n}}{\eta_g + \eta_l} = \frac{C}{\eta_g + \eta_l}, \tag{1}$$

where the constant C' captures the geometry of the system. Since in what follows we have constant driving pressure and assume time-averaged quantities, and we replace $C'(\Delta P)^{1/n}$ by a fitting parameter, C.

We assume that the global viscosity η_g is unaffected by the vibration *i.e.* it originates from wall drag or any similar effect. The local viscosity η_l includes the part of the dissipation due to local yield events, the T1 type neighbour swap events, that are triggered by the sinusoidal vibration. The local viscosity might also include changes in boundary dissipation. A suitable model is then an energy landscape model where the vibration cycle kicks the system with a finite probability of creating local rearrangements. These events are in fact fluidizing the system locally and seen as an increase in the flow rate. Thus, we turn to a Guzman–Arrhenius like model

$$\eta_l = \eta_0 \exp\left(\frac{\Delta E - E_f}{RT}\right), \tag{2}$$

where the local viscosity is reduced due to a small energy barrier of size $\Delta E - E_f$.[42,43] Here, the constant ΔE should be related to a typical barrier for T1 events and thus it determines the flow velocity without vibrations $(1/v_{\max} + 1/v_0)^{-1}$ as we will show later in the paper. E_f is the change in the energy barrier due to the vibration imposed on the system. Here, we assume that the change in energy barrier $E_f/RT \propto (f/\langle f\rangle)^2$ is proportional to the square of number of vibrations per second f. Here T notes the effective mechanical temperature similar to the kinematic granular temperature in hard sphere ensembles and R its constant scaling factor similar to Boltzmann's constant.[44,45] In the following we note the vibration independent barrier size by normalization factor $\eta_0' = \eta_0 \exp(\Delta E/RT)$.

Substituting the local viscosity (2) to the flow rate (1), one obtains

$$vA = \frac{C}{\eta_g + \eta_0' \exp\left(-(f/\langle f\rangle)^2\right)}, \tag{3}$$

where the velocity $v = Q/A$ is the volume flow rate through the cross sectional area A of the region of interest. Rearranging terms, we obtain an expression for the velocity

$$v = \left(\frac{1}{v_{\max}} + \frac{1}{v_0}\exp\left[-\left(\frac{f}{\langle f\rangle}\right)^2\right]\right)^{-1}. \tag{4}$$

The $v_{\max}$ and v_0 are fitting parameters defining the maximum and minimum velocities given by

$$v_{\max} = \frac{C}{A\eta_g} \propto \eta_g^{-1}, \quad v_0 = \frac{C}{A\eta_0 \exp(\Delta E/RT)} \propto \eta_0^{-1}. \tag{5}$$

The fit parameter $v_{\max}$ thus depends on the global viscosity η_g unaffected by the vibration and the constants C and A. The second fitting parameter v_0 depends on the same parameters as $v_{\max}$ and additionally on the size of the energy barrier of a single T1 event $\eta_0 \exp(\Delta E/RT)$. Fig. 4a shows the fit obtained using the nonlinear fitting procedure in Matlab. Here we can estimate the asymptotic behavior of $v_{\max}$ = 326 μm s^{-1} with

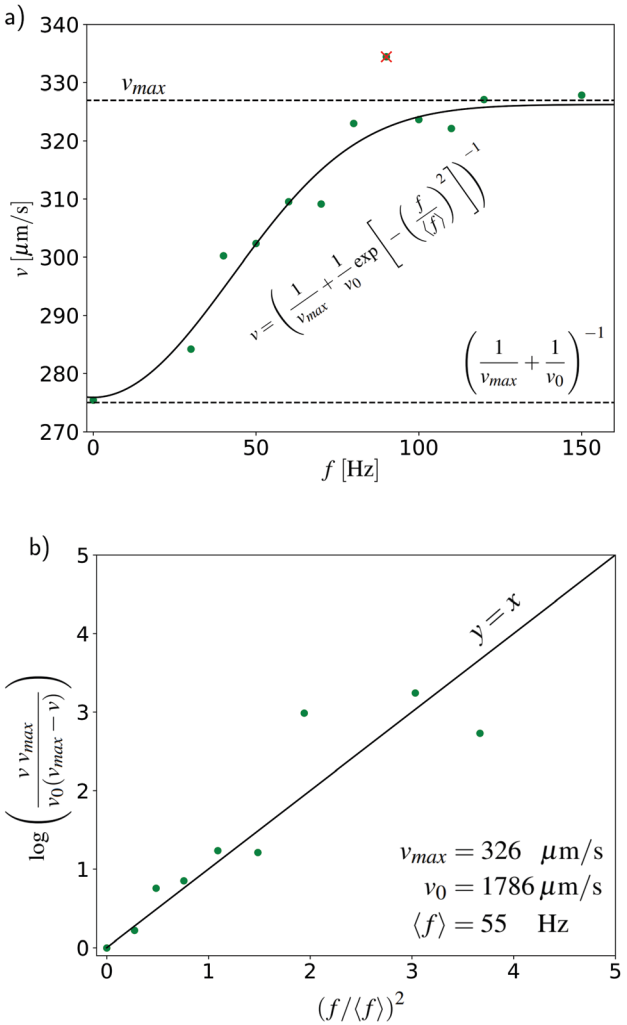

Fig. 4 (a) Frequency *vs.* flow velocity (green dots) averaged over the total time of the experiment with the given frequency (see legends in Fig. 3a). Using a Guzman–Arrhenius model, the relation between the variables is exponential. The measurement point marked by a cross has been neglected from the fitting as an outlier. (b) Linear relation of the data according to eqn (6). Note that points bigger than v_{max} are not included.

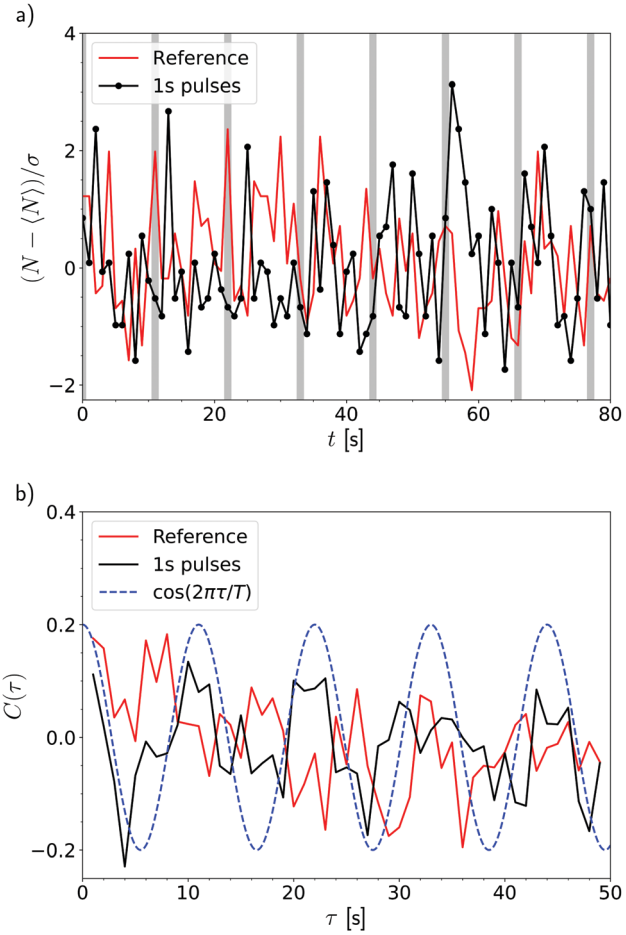

Fig. 5 (a) Number of T1 events without pulse (red line) and with pulse (black line). 30 Hz pulses of 1 s length were induced every 10 s (vertical grey bars). The data averages are shifted to zero and the curves are scaled by the standard deviation. (b) Autocorrelation function $C(\tau)$ for both datasets in (a). When the pulse is applied, there exists a correlation with the number of yielding events (black line). The dashed blue line shows the periodicity of T = 11 s in the autocorrelation function.

maximum vibration and compare it to the unvibrated case with velocity v_{min} = 276 μm s^{-1}. The gain in velocity obtained by vibration is Δv = 50 μm s^{-1} or 18% which is essentially the ratio of the two fit parameters, or the viscosities caused by the energy barrier of the T1 event and global viscosity $v_{max}/v_0 = \eta_0 \exp(\Delta E/RT)/\eta_g$ = 18%. The third fitting parameter, the scaling for the energy barrier, is $\langle f\rangle$ = 55 Hz. We expect that v_0 and $\langle f\rangle$ depend on the frequency amplitude.

As the frequency increases, the energy barrier to trigger a plastic event decreases and velocity v of the flow increases. Fig. 4a shows that the previous expression fits perfectly to the data. After rearranging eqn (4), we obtain the form

$$\left(\frac{f}{\langle f\rangle}\right)^2 = \log\left(\frac{v v_{max}}{v_0(v_{max} - v)}\right), \quad (6)$$

which is a linear relation as shown in Fig. 4b. Note that some of the measured velocities shown in Fig. 4a are larger than v_{max}. These points are omitted from Fig. 4b since at values larger than v_{max} eqn (6) results in complex numbers. The results presented in Fig. 3 and 4 indicate that the vibration indeed affects the local yielding. Next, we want to confirm our hypothesis by measuring the T1 neighbor swap events directly.

3.3 Frequency triggered yielding

To investigate the effect of vibration on the number of T1 events in a foam, an experiment with vibration pulses of one second duration was performed. The aim was to see if the vibration pulses cause local foam yielding manifested by an increase in the number of neighbor swapping events.

The T1 event detection is performed by skeletonizing the images to obtain binary data. As seen in Fig. 2a, the liquid films are darker areas in the images of the experiment. The image gray-levels are thresholded to extract the liquid films from the bubbles producing binary images. Binary images are then skeletonized. The bubble film is now seen as a one pixel wide

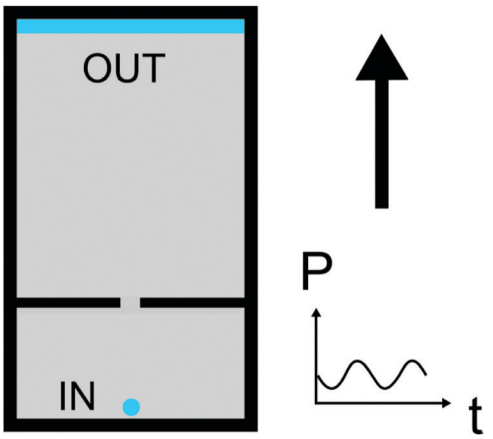

Fig. 6 Experimental setup in the auxiliary experiment. The circular inlet hole of the foam is marked by a blue circle and the open outlet region is marked by a blue line. The schematic graph illustrates the sinusoidal oscillation of the pressure.

black line on a white background allowing us to uniquely label all the bubbles and their neighboring bubbles. Next, we compare the neighbor list of each bubble between two sequential images. We identify the T1 events based on changes in the neighbor lists. The same procedure was used previously in ref. 2 and 13

Triggering events were performed by inducing 30 Hz pulses during 1 s in the foam every 10 seconds. Fig. 5a shows that the number of T1 events $N_{T1}(t)$ in the foam increases (black line) after each pulse (vertical grey bars). In contrast, no periodicity in the number of T1 is observed for the reference case (red line).

In order to confirm the periodicity in the observed number of T1 events $N_{T1}(t)$, we compute the autocorrelation functions $C(\tau)$ for both cases. Fig. 5b shows both the autocorrelation functions together with a sinusoidal wave of period $T = 11$ s (blue dashed line) highlighting the pulsing period. We clearly observe a correlation in the vibrated case (black line).

3.4 Oscillating pressure

To confirm the autocorrelation result described in the previous section, we create a new experimental setup where we vibrate a hopper-inspired geometry[28,46] driving it by an oscillating pressure difference. We use the same experimental conditions as those in the previous experiment, that is vibration amplitude and liquid fraction. Here the mean value of driving pressure corresponds to the constant pressure in the radial injection geometry. Fig. 6 shows this experimental setup, in which the foam flow is confined by placing a narrow opening in the Hele-Shaw cell. Here, the decreasing pressure eventually drops the local stress near the opening below the foam's yield stress and the flow stops in the non-vibrated case. This allows us to observe the effect of frequency by monitoring the minimum velocity near the opening, enabling direct comparisons between the vibrated and non-vibrated cases.

The behaviour of the foam flow in the presence of sinusoidal external pressure was studied by performing two experiments,

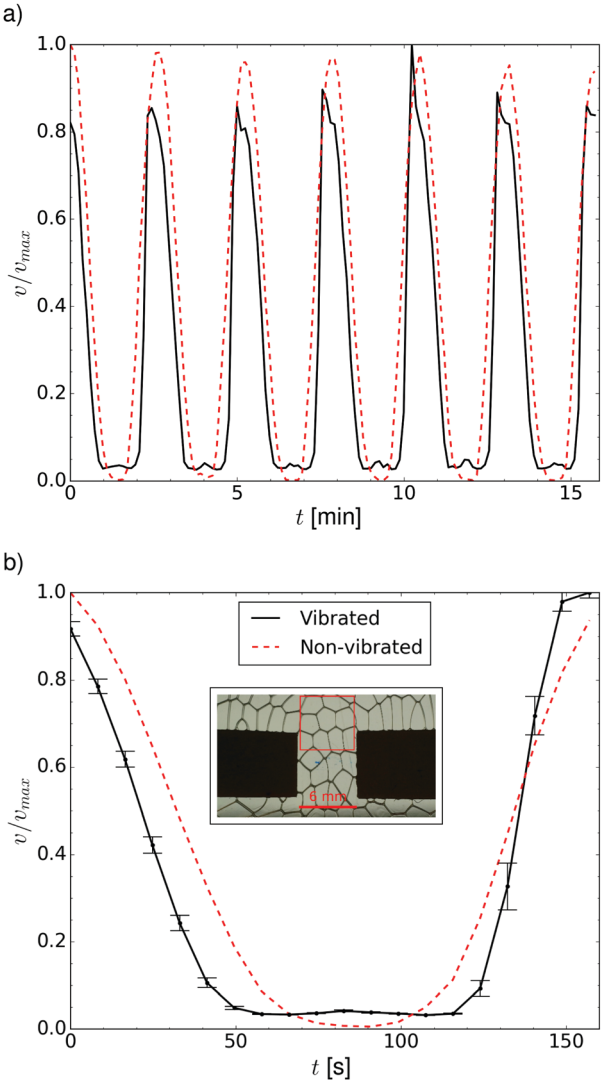

Fig. 7 Experiment with sinusoidal pressure. In (a) flow rate never goes to zero in the vibrated case (black line), in contrast to the non-vibrated case (dashed red line). In (b) all periods in the experiment are averaged in one period. The same result can be seen in this figure. Flow rate seems to react quicker to change in external pressure in the vibrated case, but foam flow rate never goes to zero.

one with mechanical vibration and another with no vibration. By trial and error, the vibration frequency in the vibrated case was set to 70 Hz. The duration of both experiments was 60 minutes, during which the pressure oscillated 24 times. The velocity analysis for the flowing foam was done using the PIV technique described in Section 3.1. Parts of the periods from both experiments are shown in Fig. 7a. Furthermore, the single period mean flow rate for both cases was determined by averaging the data from all measured periods. Graphs for mean flow rates for both vibrated and non-vibrated cases are shown in Fig. 7b.

The velocity does not fall exactly to zero in the vibrated case as can be seen in Fig. 7. In the non-vibrated case, however, the velocity goes to zero as the external pressure reaches its minimum. Thus, vibration indeed seems to lower the local yield stress in the foam

which leads to observing constantly the flowing foam in the vibrated case even when the external pressure reaches its minimum value.

The supplementary Video 1 (ESI†) shows the raw data of Fig. 7 side by side for the vibrated and non-vibrated case. The difference in flow rates is also observable by the naked eye.

4 Conclusions

We have performed novel experiments where we measure the effect of mechanical vibration on radially expanding foam flow. We observe a relation between the foam velocity and the frequency applied in the system, as is shown in Fig. 4. Effectively, we conclude that the frequency dependence of foam flow in the present experimental setup agrees with an energy landscape model. However, more general conclusions would require testing the results with varying control parameters, such as bubble size, flow rate, and liquid fraction, which could not be carried out within the current study due to complications related to foam preparation, which causes complex coupling between bubble size, polydispersity, and foam coarsening. The continuous vibrations decrease the local energy barriers leading to an increase in T1 yield event rate and the observed increase in the flow rate. We do not expect that the vibration with the present sound pressure level alone triggers T1 events. Here, the foam is already in a stressed state due to anisotropic external driving and the vibrations merely lower the local energy barrier for the T1 events. Therefore, in a relaxed foam sample, the vibration would not likely cause any deformation, so the presence of a bias stress field is essential for the observed behavior. The probability of local neighbor swaps, and the local geometry fluctuations thus define the deformation rate of the system.[47] The limiting maximum value of the flow velocity is reached, when the part of the viscosity related to the local geometrical rearrangements reaches zero.

In addition to the increment in the foam velocity, the applied frequency increases the number of neighbour swaps, facilitating the local yielding. A clear correlation between the number of T1 events and the applied frequency was observed. Finally, an experimental setup with different geometries was implemented where the difference can be observed from the raw data by the naked eye. Using the oscillating driving pressure, vibration was shown to increase the flow rate of the foam at low driving pressures.

Here, using the vibrations, we manipulate the areas of high local fluid fractions, *i.e.* the nodes, which are the key for enabling foam deformation. This contrasts the case of flowing granular media, where vibrations induce the motion of particles, which leads to a decrease in the local particle fraction, unjamming the system locally.[33] Here however, the global volume fraction will not change due to volume conservation. Due to the lack of direct evidence, we are inclined to think that since due to geometrical restrictions, other degrees of freedom are suppressed in our system, the effect observed might be due to slight variations in the local fluid concentrations, which lower the yield stress locally. Despite such differences, our study aligns nicely with the observations involving granular media, where the particle packing fraction,[48,49] and vibration[50] as well as the interstitial medium[51,52] can be shown to affect the flow rate and the clogging probability.

In the future, in addition to a more detailed investigation of the current experiment's control parameters, we would like to extend these studies to emulsions and tune the interaction and thus the energy barrier height in particle laden foams. Also, a more detailed analysis of differences between T1 events in vibrated *versus* non-vibrated experiments could reveal a possible characteristic event timescale dependence on the frequency.[53] Additionally, the cyclic experiment allows for studying the memory effects related to T1 events.

Conflicts of interest

There are no conflicts to declare.

Acknowledgements

The authors acknowledge support from the Academy of Finland Center of Excellence program, 278367. JK and AP acknowledge the funding from the Academy of Finland (308235 and 278367) and the FinnCERES flagship program, Business Finland (211715) and Aalto University (974109903) as well as the Aalto Science IT project for computational resources. LV acknowledges the funding from the Vilho, Yrjö and Kalle Väisälä Foundation *via* a personal grant.

Notes and references

1 A. Nicolas, E. E. Ferrero, K. Martens and J.-L. Barrat, *Rev. Mod. Phys.*, 2018, **90**, 045006.
2 L. Viitanen, J. Mac Intyre, J. Koivisto, A. Puisto and M. Alava, *Phys. Rev. Res.*, 2020, **2**, 023338.
3 O. Pitois and F. Rouyer, *Curr. Opin. Colloid Interface Sci.*, 2019, **43**, 125–137.
4 P. Coussot, *Rheol. Acta*, 2018, **57**, 1–14.
5 C. Raufaste, B. Dollet, K. Mader, S. Santucci and R. Mokso, *EPL*, 2015, **111**, 38004.
6 A. Basu, Y. Xu, T. Still, P. Arratia, Z. Zhang, K. Nordstrom, J. M. Rieser, J. Gollub, D. Durian and A. Yodh, *Soft Matter*, 2014, **10**, 3027–3035.
7 A. C. Barbati, J. Desroches, A. Robisson and G. H. McKinley, *Annu. Rev. Chem. Biomol. Eng.*, 2016, **7**, 415–453.
8 T. Härkäsalmi, J. Lehmonen, J. Itälä, C. Peralta, S. Siljander and J. A. Ketoja, *Cellulose*, 2017, **24**, 5053–5068.
9 J. Ketoja, E. Hellén, J. Lappalainen, A. Kulachenko, A. Puisto, M. Alava, A. Penttilä, K. Lumme, S. Paavilainen, T. Róg, I. Vattulainen, D. Vidal and T. Uesaka, *International Conference on Nanotechnology for the Forest Products Industry 2010*, TAPPI Press, Espoo, 2010.
10 D. Bonn, M. M. Denn, L. Berthier, T. Divoux and S. Manneville, *Rev. Mod. Phys.*, 2017, **89**, 035005.

11 L. Viitanen, J. Koivisto, A. Puisto, M. Alava and S. Santucci, *Eur. Phys. J. B*, 2019, **92**, 38.
12 L. Viitanen, A. Halonen, E. Friström, J. Koivisto, M. Korhonen, A. Puisto and M. Alava, *BioResources*, 2019, **14**, 5716–5728.
13 B. Dollet and F. Graner, *J. Fluid Mech.*, 2007, **585**, 181–211.
14 I. Cheddadi, P. Saramito, B. Dollet, C. Raufaste and F. Graner, *Eur. Phys. J. E: Soft Matter Biol. Phys.*, 2011, **34**, 1.
15 A. T. Chieco, M. Zu, A. J. Liu, N. Xu and D. J. Durian, *Phys. Rev. E*, 2018, **98**, 042606.
16 A. M. Al-Qararah, A. Ekman, T. Hjelt, J. A. Ketoja, H. Kiiskinen, A. Koponen and J. Timonen, *Colloids Surf., A*, 2015, **482**, 544–553.
17 M. J. Shojaei, K. Osei-Bonsu, P. Grassia and N. Shokri, *Ind. Eng. Chem. Res.*, 2018, **57**, 7275–7281.
18 D. Kong, Y. Li, M. Yu, R. Ma, H. Guo, Y. Peng, S. Xu and H. Yan, *Colloids Surf., A*, 2019, **570**, 22–31.
19 S. Cohen-Addad, R. Höhler and O. Pitois, *Annu. Rev. Fluid Mech.*, 2013, **45**, 241–267.
20 A. Maestro, E. Rio, W. Drenckhan, D. Langevin and A. Salonen, *Soft Matter*, 2014, **10**, 6975–6983.
21 D. Weaire and S. Hutzler, *The Physics of Foams*, Oxford University Press Inc., New York, 2001.
22 D. Weaire and R. Phelan, *Philos. Mag. Lett.*, 1994, **69**, 107–110.
23 M. L. Falk and J. S. Langer, *Phys. Rev. E: Stat., Nonlinear, Soft Matter Phys.*, 1998, **57**, 7192–7205.
24 M. L. Manning and A. J. Liu, *Phys. Rev. Lett.*, 2011, **107**, 108302.
25 T. Chevalier, J. Koivisto, N. Shmakova, M. J. Alava, A. Puisto, C. Raufaste and S. Santucci, *J. Phys.: Conf. Ser.*, 2017, **925**, 012025.
26 B. Dollet, F. Elias, C. Quilliet, C. Raufaste, M. Aubouy and F. Graner, *Phys. Rev. E: Stat., Nonlinear, Soft Matter Phys.*, 2005, **71**, 031403.
27 M. V. Hecke, *J. Phys.: Condens. Matter*, 2010, **22**, 033101.
28 C. C. Thomas and D. J. Durian, *Phys. Rev. Lett.*, 2015, **114**, 178001.
29 D. A. Huerta and J. C. Ruiz-Suárez, *Phys. Rev. Lett.*, 2004, **92**, 114301.
30 H. G. Sheldon and D. J. Durian, *Granul. Matter*, 2010, **12**, 579–585.
31 A. R. Abate and D. J. Durian, *Phys. Rev. E*, 2006, **74**, 031308.
32 B. Ferdowsi, C. P. Ortiz, M. Houssais and D. J. Jerolmack, *Nat. Commun.*, 2017, **8**, 1363.
33 A. Gnoli, L. De Arcangelis, F. Giacco, E. Lippiello, M. P. Ciamarra, A. Puglisi and A. Sarracino, *Phys. Rev. Lett.*, 2018, **120**, 138001.
34 Y. Zhao, J. Ding, J. Barés, H. Zheng, K. Dierichs, A. Menges and R. Behringer, *EPJ Web Conf.*, 2017, **140**, 06011.
35 S. Ogawa, A. Umemura and N. Oshima, *Z. Angew. Math. Phys.*, 1980, **31**, 483–493.
36 L. J. Daniels, T. K. Haxton, N. Xu, A. J. Liu and D. J. Durian, *Phys. Rev. Lett.*, 2012, **108**, 138001.
37 A. R. Abate and D. J. Durian, *Phys. Rev. Lett.*, 2008, **101**, 245701.
38 N. Menon and D. J. Durian, *Science*, 1997, **275**, 1920–1922.
39 Y. Gai, A. Bick and S. K. Tang, *Phys. Rev. Fluids*, 2019, **4**, 014201.
40 W. Thielicke and E. Stamhuis, *J. Open Res. Softw.*, 2014, **2**, 30.
41 I. Ben Salem, I. Cantat and B. Dollet, *J. Fluid Mech.*, 2013, **714**, 258–282.
42 C. E. Waring and P. Becher, *J. Chem. Phys.*, 1947, **15**, 488–496.
43 M. lezak, *Arch. Metall. Mater.*, 2015, **60**, 581–589.
44 I. K. Ono, C. S. O'Hern, D. J. Durian, S. A. Langer, A. J. Liu and S. R. Nagel, *Phys. Rev. Lett.*, 2002, **89**, 095703.
45 H. M. Jaeger, C.-h. Liu and S. R. Nagel, *Phys. Rev. Lett.*, 1989, **62**, 40–43.
46 J. Koivisto, M. Korhonen, M. Alava, C. P. Ortiz, D. J. Durian and A. Puisto, *Soft Matter*, 2017, **13**, 7657–7664.
47 M. Le Goff, E. M. Bertin and K. Martens, *JPhys Mater.*, 2020, **3**, 025010.
48 A. Garcimartín, J. M. Pastor, L. M. Ferrer, J. J. Ramos, C. Martín-Gómez and I. Zuriguel, *Phys. Rev. E: Stat., Nonlinear, Soft Matter Phys.*, 2015, **91**, 022808.
49 R. O. Uñac, A. M. Vidales and L. A. Pugnaloni, *J. Stat. Mech.: Theory Exp.*, 2012, P04008.
50 A. Janda, D. Maza, A. Garcimartín, E. Kolb, J. Lanuza and E. Clément, *Europhys. Lett.*, 2009, **87**, 24002.
51 J. Koivisto and D. J. Durian, *Nat. Commun.*, 2017, **8**, 15551.
52 J. Koivisto and D. J. Durian, *Phys. Rev. E*, 2017, **95**, 032904.
53 A. Baldassarri, M. Annunziata, A. Gnoli, G. Pontuale and A. Petri, *Sci. Rep.*, 2019, **9**, 1–10.

